

# Linear and nonlinear reconstruction for optical tomography of phantoms with nonscattering regions

Adam P. Gibson, Jeremy C. Hebden, Jason Riley, Nicholas Everdell, Martin Schweiger, Simon R. Arridge, and David T. Delpy

Most research in optical imaging incorrectly assumes that light transport in nonscattering regions in the head may be modeled by use of the diffusion approximation. The effect of this assumption is examined in a series of experiments on tissue-equivalent phantoms. Images from cylindrical and head-shaped phantoms with and without clear regions [simulating the cerebrospinal fluid (CSF) filled ventricles] and a clear layer (simulating the CSF layer surrounding the brain) are reconstructed with linear and nonlinear reconstruction techniques. The results suggest that absorbing and scattering perturbations can be identified reliably with nonlinear reconstruction methods when the clear regions are also present in the reference data but that the quality of the image degrades considerably if the reference data does not contain these features. Linear reconstruction performs similarly to nonlinear reconstruction, provided the clear regions are present in the reference data, but otherwise linear reconstruction fails. This study supports the use of linear reconstruction for dynamic imaging but suggests that, in all cases, image quality is likely to improve if the clear regions are modeled correctly. © 2005 Optical Society of America  
*OCIS codes:* 170.3880, 170.6920.

## 1. Introduction

Optical tomography is a medical imaging technique in which near-infrared (NIR) light is used to interrogate tissue noninvasively.<sup>1–3</sup> If appropriate measurements are taken from multiple source and detector positions, images of both the absorption and the scatter properties of tissue can be reconstructed. The primary absorbers include oxyhemoglobin and deoxyhemoglobin, which have different absorption spectra at NIR wavelengths, allowing blood oxygenation to be determined spectroscopically. Clinically, optical tomography has been used to image the breast,<sup>4–8</sup> the neonatal brain,<sup>9–11</sup> and to map adult cortical brain function.<sup>12–14</sup> A major motivation for the development of optical tomography in our group at University College London (UCL) is to monitor cerebral hypoxic-ischemic in-

jury in term and preterm infants noninvasively at the bedside.<sup>15</sup>

Even though most clinical information is contained in the characteristic absorption of tissues, scatter is generally the dominant effect. Indeed, in most tissue we can assume that the transport scatter coefficient ( $\mu_s'$ ) is much greater than the absorption coefficient ( $\mu_a$ ), so the direction of travel of a photon is random once it has traveled a few millimeters through tissue. This means that rather than modeling light propagation using the full radiative transport equation, which is computationally expensive, we instead assume that light can be modeled in most tissues as a diffusive process.<sup>1</sup> However, this assumption breaks down in some parts of the model, such as close to the sources and detectors, near boundaries, in large blood vessels, and in regions that are filled with clear, nonscattering fluids.<sup>16</sup> The cerebrospinal fluid (CSF) that both surrounds the brain and fills the ventricles in its center is primarily clear water with some dissolved salts, so it is incorrect to assume that light propagation in the CSF is diffusive. Despite this, many groups have published useful data from the head using NIR spectroscopy,<sup>17–19</sup> topography<sup>12–14,20</sup> and tomography<sup>9–11</sup> without correctly accounting for the nonscattering regions. These data have been validated against other techniques,<sup>21,22</sup> so it appears that, although neglecting the nonscattering regions

---

A. P. Gibson (agibson@medphys.ucl.ac.uk), J. C. Hebden, N. Everdell, and D. T. Delpy are with the Department of Medical Physics and Bioengineering, University College London, London WC1E 6JA, United Kingdom. J. Riley, M. Schweiger, and S. R. Arridge are with the Department of Computer Science, University College London, London WC1E 6BT, United Kingdom.

0003-6935/05/193925-12\$15.00/0

© 2005 Optical Society of America

can never give perfect results, the error is small enough for clinically useful images to be obtained.

The effect of nonscattering regions on light transport in optical imaging has been examined by comparison of simulations from the diffusion equation to the full transport model,<sup>23,24</sup> Monte Carlo methods<sup>25</sup> and data measured on phantoms.<sup>26,27</sup> It has been shown that nonscattering regions significantly distort surface measurements by increasing the measured intensity and decreasing the mean photon flight time,<sup>26</sup> while also decreasing the sensitivity of surface measurements to deeper tissues.<sup>24,25</sup> Furthermore, Hielscher *et al.*<sup>23,28</sup> have shown that the diffusion equation significantly overestimates the absorption when  $(\mu_a/\mu_s') > 1/40$ .

A number of groups have also examined the effect of void regions on the image reconstruction problem. In general, two approaches have been taken: absolute imaging of simulated data, and imaging using the difference between two data sets measured on phantoms. Difference imaging is known to be much more robust to experimental and modeling errors, and corresponds clinically to imaging before and after a change in optical properties. Dehghani *et al.*<sup>24</sup> took the first approach and showed that the diffusion equation can be used to reconstruct absolute 2D images from data simulated from a model with a nonscattering layer, provided that the layer is less than 0.5 mm thick (when  $\mu_a = 0.025 \text{ mm}^{-1}$  and  $\mu_s' = 2.0 \text{ mm}^{-1}$ ). Nonscattering layers of thickness 1 mm or more, or deep, discrete nonscattering regions of 10 mm radius, prevented reliable image reconstruction.<sup>29</sup> However, images have been accurately reconstructed with the difference between data collected on a cylindrical phantom with a 3 mm thick void layer and data collected on the same phantom with void perturbations added ( $\mu_a = 0.002 \text{ mm}^{-1}$  and  $\mu_s' = 1.0 \text{ mm}^{-1}$ ).<sup>30,31</sup>

Two contrasting approaches are generally taken in optical tomography image reconstruction. Nonlinear reconstruction attempts to fit a model to the data and iteratively update the optical properties of the model until the simulated data match the measured data to within a specified tolerance.<sup>1,32</sup> Inevitably, errors occur when the model is unable to generate simulated data that match the measured data. This mismatch can arise owing to noise or error in the data, or because the model inadequately represents the object being imaged. Linear reconstruction, on the other hand, assumes that changes in optical properties from an initial, known state are small and do not significantly distort the initial distribution of light in the object.<sup>1</sup> From this, we can hypothesize that nonlinear reconstruction may be most appropriate when the model accurately represents the object and the optical properties depart significantly from a known yet “model-able” starting point, but that linear reconstruction may be more reliable if there is a small change in optical properties from less well known or less “model-able” starting conditions.

In this study, we examine this hypothesis by pre-

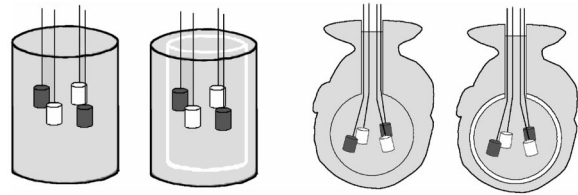


Fig. 1. Schematic diagram showing the phantoms. The hollow cylindrical phantom with and without a clear layer and the head-shaped phantom with and without a clear layer are shown with two clear regions and two diffusive perturbations. The locations and sizes of the perturbations are illustrative only and are not to scale.

sending images reconstructed from two cylindrical tissue-equivalent optical phantoms (Fig. 1). One of the two phantoms includes a smooth clear layer (to simulate the CSF), the other, when filled with liquid resin, is homogeneous. Two clear inclusions were also used (to simulate ventricles), and absorbing and scattering perturbations provided features of interest. Data were collected for various combinations of objects within each phantom (see Fig. 2) and images were reconstructed (with the diffusion approximation) by use of both linear and nonlinear techniques. This study allows the effect of discrete nonscattering regions and of a nonscattering layer on the image quality to be examined for both linear and nonlinear imaging.

We extended the research by repeating the data collection, image reconstruction, and analysis using phantoms cast in the shape of the neonatal head (Fig. 1). The clear layer simulated the CSF, and the clear inclusions represented the ventricles. This extension enabled us to examine to what extent clinical images may be influenced by the CSF and ventricles. Furthermore, we attempted to simulate the two primary applications of optical tomography in neonatal brain imaging, namely, static imaging using a diffusive medium as reference that we have used to image hemorrhage<sup>10</sup> and difference imaging before and after an induced change (which we have used to image the effect of hemodynamic changes induced by changing ventilator settings<sup>11</sup>).

## 2. Method

Four tissue-equivalent optical phantoms (Fig. 1) were built from epoxy resin<sup>33</sup>: two were cylindrical (70 mm diameter, 140 mm height) with a hollow center (60 mm in diameter), and two were cast from a mold made from an anatomically realistic doll, corresponding to a baby of ~26 weeks gestation.<sup>34</sup> The head-shaped phantoms contained a hollow sphere of diameter 56 mm. The optical properties of the resin were adjusted with titanium dioxide (for scatter) and a NIR absorbing dye to give nominal background properties of  $\mu_a = 0.01 \text{ mm}^{-1}$  and  $\mu_s' = 1.0 \text{ mm}^{-1}$ . The hollow center of one of the cylindrical phantoms and one of the head-shaped phantoms was coated with a 1 mm shell of clear resin without scatterers or absorbing dye to act as a clear layer. The actual ab-

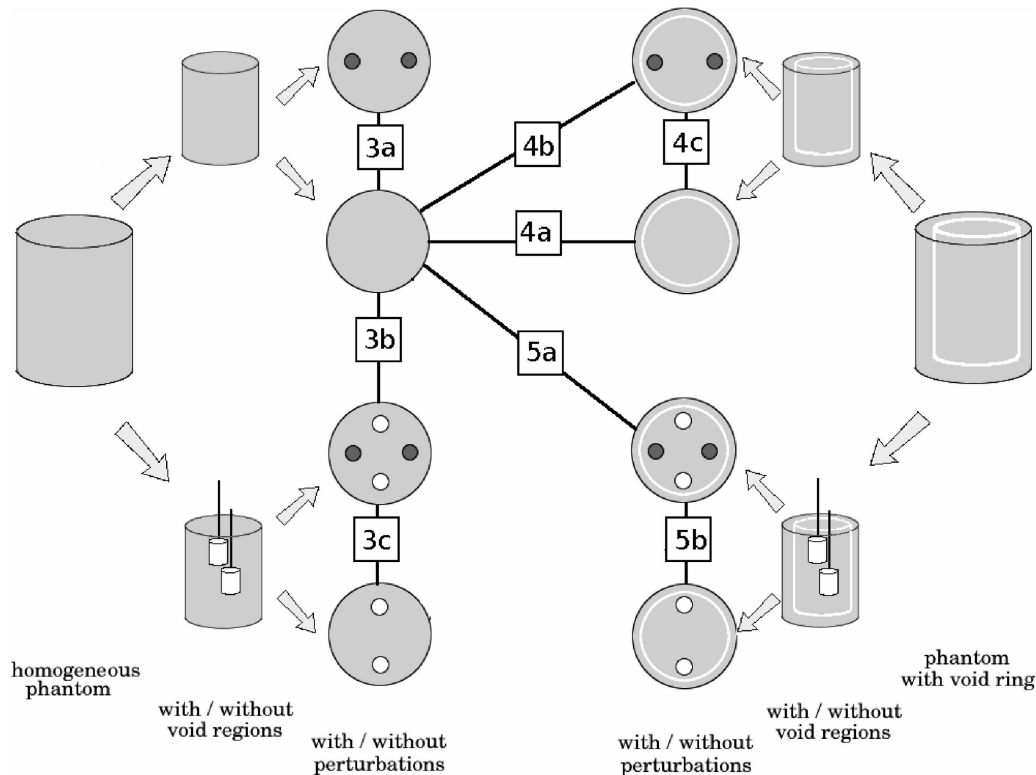


Fig. 2. Schematic diagram showing the reconstruction combinations. On the left is the homogeneous phantom, with or without clear regions, and finally transverse slices through the phantom with or without two diffusive perturbations. From the right are the equivalent combinations in the phantom with a clear layer. Clear regions are white; diffusive regions gray. The labels on the central network of solid lines refer to the imaging combinations, the results of which are shown in Figs. 3 to 5.

sorption  $\mu_a$  was  $0.002 \text{ mm}^{-1}$  and the scatter was negligible. The hollow centers of all four phantoms were filled with liquid epoxy resin (i.e., without hardener) with identical optical properties to those of the surrounding solid phantom. Two diffusive perturbations for each phantom (one with  $5\times$  background  $\mu_a$  and  $\mu_s'$  and one with  $5\times$  background  $\mu_s'$  for the cylindrical phantom, and one with  $5\times$  background  $\mu_a$  and one with  $5\times$  background  $\mu_s'$  for the head-shaped phantom) and two clear perturbations (each a 7 mm diameter cylinder, 7 mm high) were made from solid epoxy resin and supported on thin wire. The refractive index  $n$  of the outer solid layer, the clear layer, the liquid resin, and the perturbations were the same to within 1% ( $n = 1.56$  at 780 nm). Although imaging the head-shaped phantom has the potential to provide the most reliable indication of the effect of the nonscattering regions on clinical images, image reconstruction from an object with such a complex shape introduces other potential problems owing to finite-element modeling errors and imprecise knowledge of the positions of the optical connectors. Consequently, reconstructing images from the cylindrical phantom is a more reliable method and allows the effect of the void region to be examined independently of other potential sources of error.

Data were obtained with our time-resolved optical imaging system known as Multi-channel Optoelectronic Near-infrared System for Time-resolved

Image Reconstruction (MONSTIR).<sup>10,35</sup> A portable fiber laser (IMRA Inc.) produces pulses of 2 ps duration at 780 and 815 nm, interlaced at 80 MHz with total power at the source tip of 15 mW. An optical switch couples these pulses to one of 32 locations on the surface of the phantom. Each source fiber runs along the central axis of a combined source–detector bundle with the detector fibers surrounding the source and optically isolated from it. For the cylindrical phantoms, the 32 sources were held in 4 rings of 8 sources each, while a custom-built helmet was used for the head-shaped phantoms.<sup>10,34</sup> The whole fiber bundle is held 10 mm from the surface of the phantom by a connector.<sup>36</sup>

Each source is illuminated in turn for 10 s, and each detector collects light that has diffused through the phantom. The detector fiber bundles are coupled to four 8-anode microchannel plate photomultiplier tubes (MCP-PMTs) that are protected from overexposure by programmable variable optical attenuators. The MCP-PMTs produce an electrical pulse when a photon is detected. Their time of arrival is compared with a reference pulse from the laser to give the time taken for each detected photon to diffuse across the phantom. Many such measurements are collected to give a histogram of photon flight times (or temporal point-spread functions, TPSFs) for each source–detector pair. The TPSFs are processed to give time-domain datatypes such as intensity and

mean photon flight time, or the log amplitude and phase of the Fourier transform of the TPSF.<sup>1</sup>

Data were acquired from the cylindrical phantoms for a range of configurations shown in Fig. 2. In all cases, the inclusions (whether clear or diffusive) were positioned in the central plane.

Finite element meshes for use in the image reconstruction were produced by use of Netgen<sup>37</sup> by modeling the cylinder with constructive solid geometry and taking the surface of the head-shaped phantom from a CT image.<sup>34,38</sup> A mesh was deemed to be acceptable if it produced simulated maps of photon density and mean flight time that were positive and smooth everywhere.

Images were reconstructed with both linear and nonlinear techniques. For linear reconstruction, the problem was linearized with the Rytov approximation such that changes in the measurements  $\mathbf{y}$  were related to changes in the optical properties  $\mathbf{x}$  by the matrix equation  $\mathbf{y} = \mathbf{A}\mathbf{x}$ , where  $\mathbf{A}$  is the sensitivity matrix.<sup>39</sup> Images of the optical properties  $\mathbf{x}$  were then generated by Tikhonov regularization of the Moore–Penrose generalized inverse  $\mathbf{x} = \mathbf{A}^T(\mathbf{A}\mathbf{A}^T + \lambda\mathbf{I})\mathbf{y}$ . The sensitivity matrix  $\mathbf{A}$  was found by solution of the diffusion equation with the finite-element method for an initial estimated distribution of optical properties. Complications arise because  $\mathbf{y}$  consists of measurements of both log amplitude and phase, and  $\mathbf{x}$  includes images of both  $\mu_a$  and  $\mu_s'$ . These have different scales and, in the case of the data, even different dimensions, so before inversion,  $\mathbf{y}$  and  $\mathbf{A}$  were normalized by division by the mean optical parameters. Regularization was performed by adjustment of the parameter  $\lambda$ , which in this work was set at 1% of the maximum singular value of  $\mathbf{A}\mathbf{A}^T$ . A range of  $\lambda$  from  $10^{-4}$  to 1 was examined. A value of 0.01 appeared to give smooth, relatively artifact-free images and corresponds to a mismatch between the data and the model of 1%, which is similar to the predicted uncertainties.

The same sets of difference data were also reconstructed with the nonlinear time-resolved optical absorption and scattering tomography (TOAST) reconstruction scheme, developed at UCL.<sup>32,40</sup> TOAST represents the image with a finite-element model and solves the nonlinear inverse problem by iteratively adjusting the internal properties using nonlinear optimization to minimize an error norm between the model and the data. Convergence occurs when the error norm either is reduced below a specified threshold or has ceased to reduce significantly between iterations. In practice, the error norm ceased to reduce after 20 iterations, and the reconstructions were terminated at this point. In this study, images were reconstructed from the ratio of total intensity and the difference in mean photon flight time between two states.

In all cases, even when the reference phantom included a void region, the starting properties were assumed homogeneous with  $\mu_a = 0.01 \text{ mm}^{-1}$  and  $\mu_s' = 1.0 \text{ mm}^{-1}$ . This assumption is obviously incor-

rect, and it has been shown<sup>34</sup> that, if inhomogeneities are known in advance and can be included in the model, the reconstructed images can be significantly improved. However, structural images of babies [e.g., from magnetic resonance imaging (MRI)] are not routinely available, so we cannot rely on knowing the position of the void regions *a priori*.

In this study, we concentrated on examining the qualitative appearance of the images. In optical tomography, quantitative measurements of image quality such as resolution, spatial accuracy, and contrast vary between experiments. They depend on parameters such as the location of the perturbations, the number and arrangement of the connectors, and the size and optical properties of the different regions in the phantom. Therefore in this research, rather than examining quantitative measurements that might be difficult to generalize to other situations, more general, qualitative assessments have been made.

### 3. Results and Discussion

#### A. Cylindrical Phantom

Images reconstructed from data acquired on the cylindrical phantoms are presented in Figs. 3–5. Each figure consists of four rows of images along with schematic diagrams showing the position of the perturbations. The top two rows show images of absorption and scatter reconstructed nonlinearly; the bottom two rows show the corresponding linear reconstructions. In all cases, the central transverse slice through a 3D image is shown.

#### 1. Clear Perturbations

Figure 3 shows the effect of clear perturbations on the image reconstruction. Figure 3(a) shows that both linear and nonlinear reconstruction techniques can resolve both diffusive perturbations in a homogeneous phantom as separate features. The linear reconstruction gave slightly better spatial resolution. In this example, as in all cases, the quantitative accuracy of the images is poor—a  $5\times$  change in optical properties produces only approximately a 10% change in the image. This poor quantitation is a feature of ill-conditioned image reconstruction without prior information and is due to the partial volume effect: the size of the feature in the image is significantly larger than the size of the perturbation and so the effect of the change in optical properties is effectively blurred over a larger volume.

Images reconstructed from data acquired when the two clear perturbations were present in the difference data but not the reference [Fig. 3(b)] show that nonlinear reconstruction can identify both the clear and the diffusive perturbations. In the absorption image, the two diffusive perturbations appear to be blurred together into a single feature and the clear regions are not visible, but encouragingly, in the scatter image, the two clear regions appear as significant decreases in scatter, and the two diffusive perturbations appear as increases in scatter. Unfortunately,

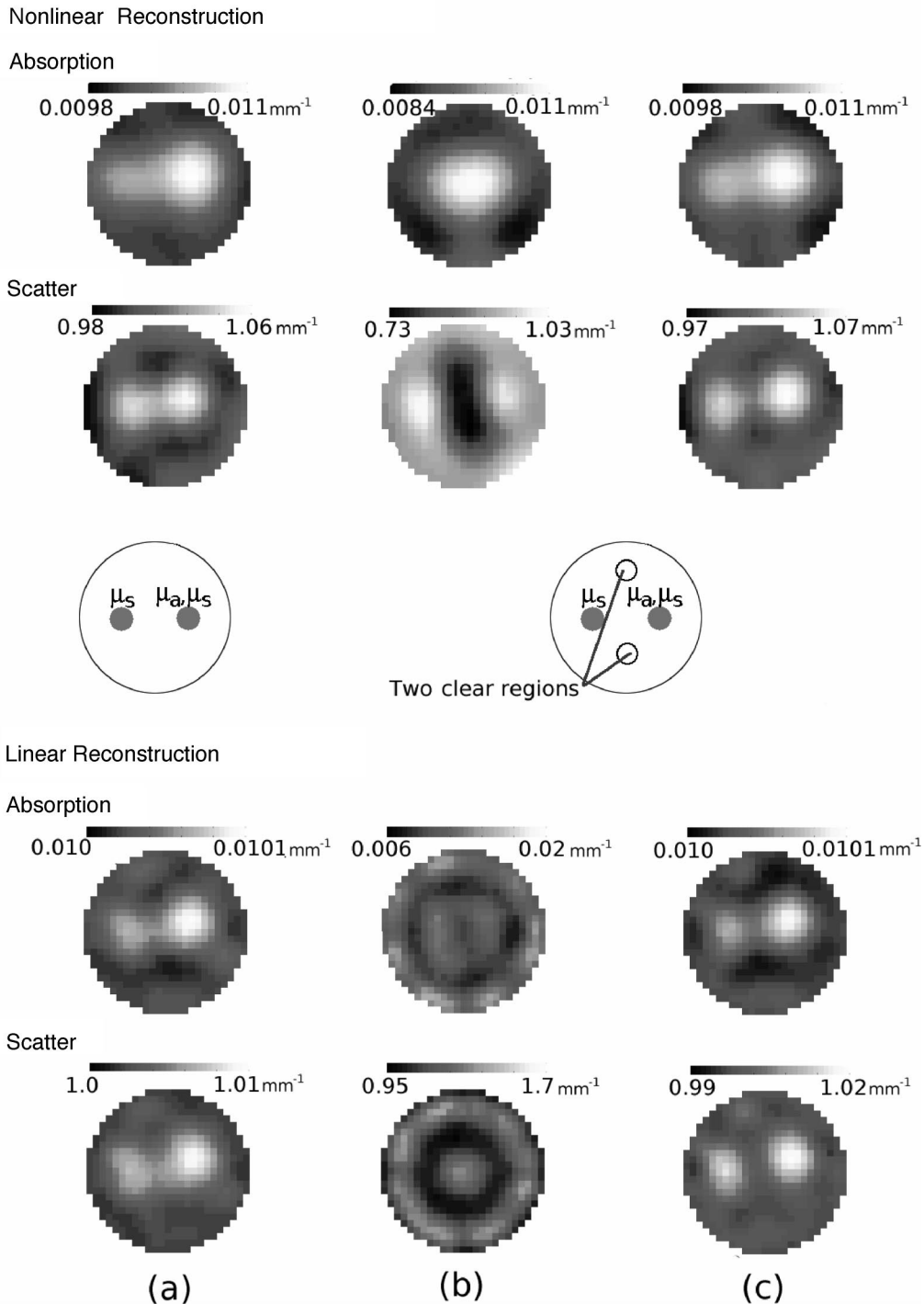


Fig. 3. Effect of clear regions. From left: (a) two perturbations in homogeneous tank, reconstructed with homogenous tank as reference; (b) two perturbations and two clear regions in homogeneous tank, reconstructed against homogenous tank; (c) two perturbations and two clear regions in homogeneous tank, reconstructed against homogenous tank with two clear regions.

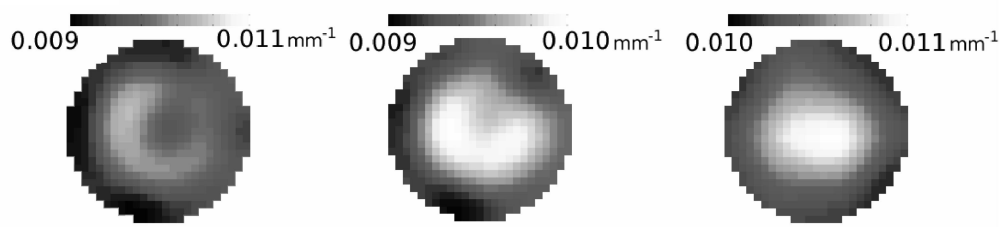
however, the linear reconstruction fails, suggesting that the initial Jacobian is significantly different from that for a homogeneous mesh. The ringlike artifact seems a typical response given by the linear reconstruction technique when the reconstruction has failed.

Figure 3(c) shows images reconstructed when the

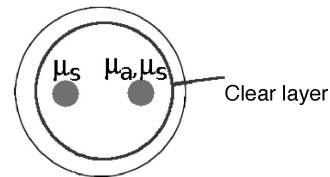
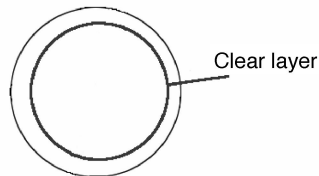
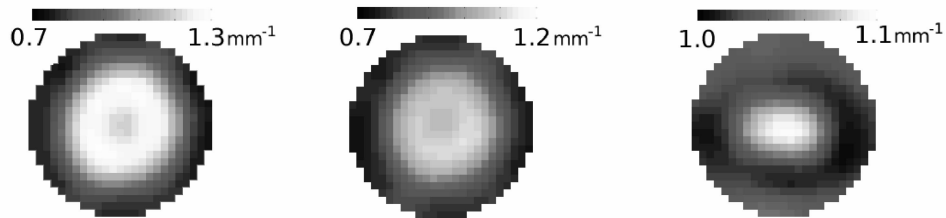
two void regions are present in both the reference and the data image sets. Both reconstruction techniques perform well, suggesting that when the void regions are present in both data sets, they tend to cancel out in the difference data. Similar results have been obtained in simulation or simple phantoms by others.<sup>39,41,42</sup>

## Nonlinear Reconstruction

### Absorption

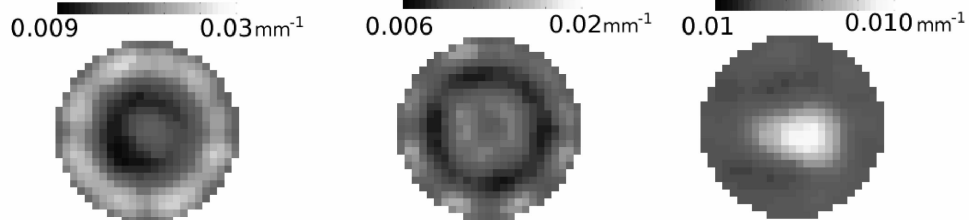


### Scatter

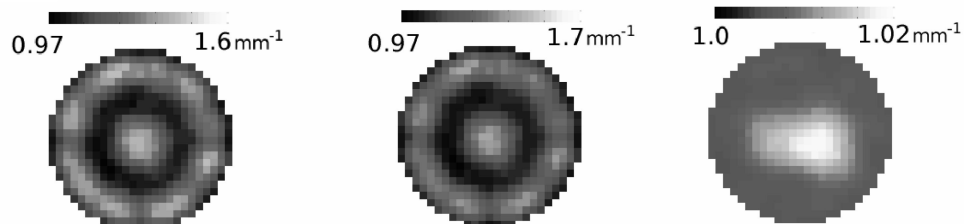


## Linear Reconstruction

### Absorption



### Scatter



(a)

(b)

(c)

Fig. 4. Effect of clear ring: (a) tank with clear ring and no perturbations, reconstructed against homogeneous tank; (b) two perturbations in clear ring, reconstructed against homogeneous tank; (c) two perturbations in clear ring, reconstructed against tank with clear ring as reference.

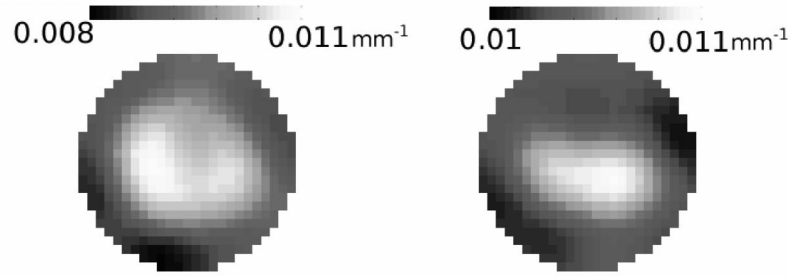
## 2. Clear Layer

Figure 4 shows images reconstructed in the presence of a 1-mm-thick smooth void layer. Figure 4(a) shows images reconstructed from the difference between the

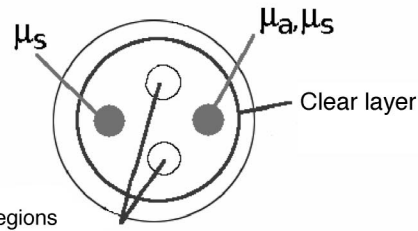
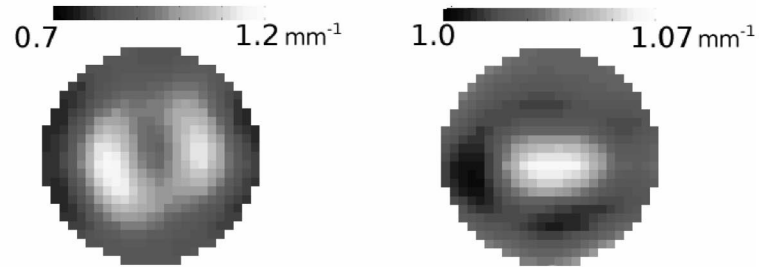
phantom with the void layer and the homogeneous phantom. The nonlinear reconstruction shows circular features, corresponding to the circular symmetry of the phantom, but no useful features can be seen.

Nonlinear Reconstruction

Absorption

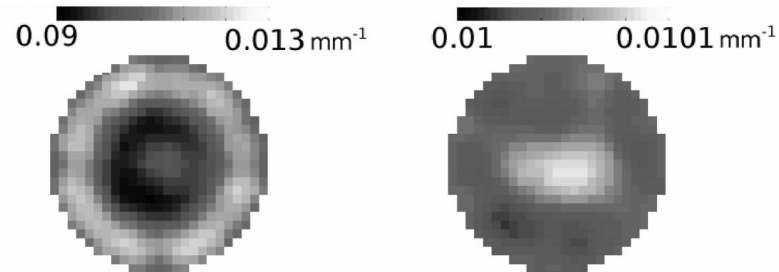


Scatter

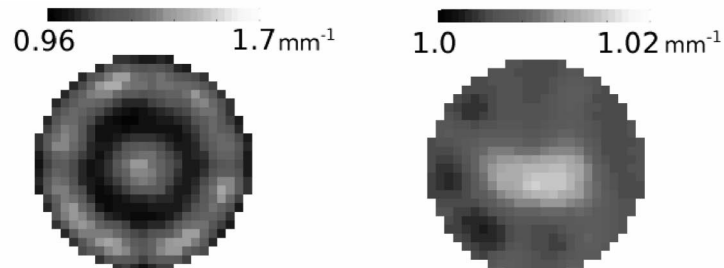


Linear Reconstruction

Absorption



Scatter

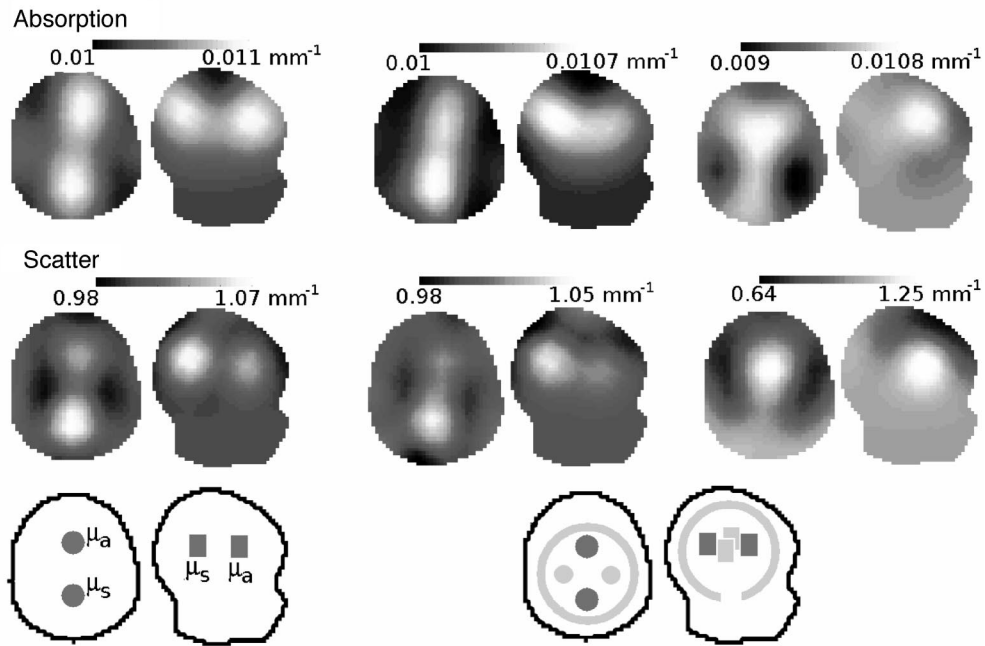


(a)

(b)

Fig. 5. Effect of clear regions and ring. Tank with perturbations in clear ring with two clear regions, reconstructed against (a) homogeneous tank; (b) tank with clear ring and clear regions; (c) homogeneous tank with clear regions.

## Nonlinear Reconstruction



## Linear Reconstruction

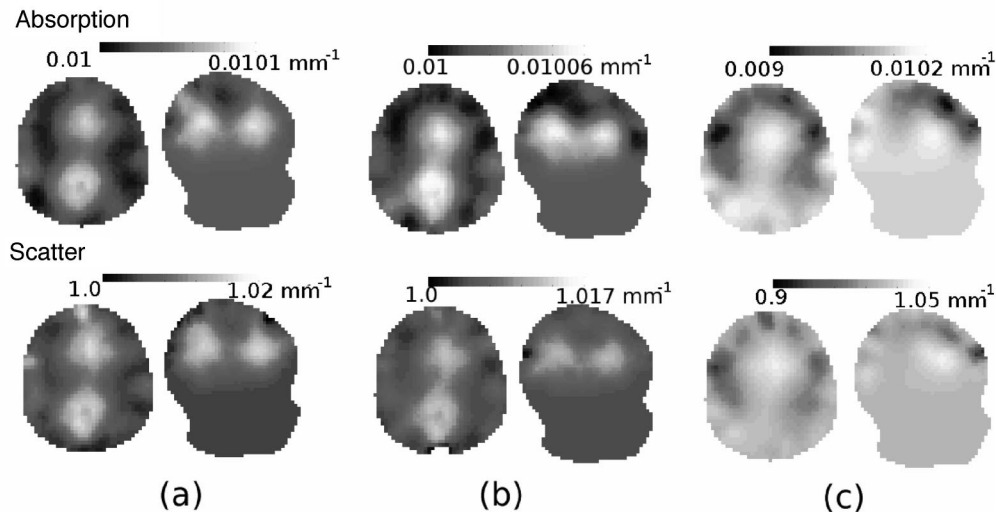


Fig. 6. Reconstructions from head-shaped phantom: (a) two diffusive perturbations in diffusive-only phantom reconstructed with homogeneous phantom as reference; (b) two diffusive perturbations placed into phantom with clear layer and two clear regions reconstructed with same phantom as reference (simulating physiological change); (c) two diffusive perturbations placed into phantom with clear layer and two clear regions reconstructed with homogeneous, diffusive-only phantom as reference (simulating static imaging with fluid-filled balloon as reference).

The void layer appears unexpectedly as a significant increase in scatter. The linear reconstruction is dominated by ringlike artifacts, indicating that the reconstruction failed.

When two diffusive perturbations are included in the phantom with the void layer, with the homogeneous phantom as reference [Fig. 4(b)], two distinct regions of increased absorption can be seen in the nonlinear reconstruction, but the spatial accuracy

and resolution are poor. Again, the linear reconstruction failed.

Figure 4(c) shows images reconstructed when the two diffusive perturbations were added to the phantom with the clear layer, and the clear layer was present in the reference data. In this case, both linear and nonlinear reconstructions show features that correlate with the inclusions, although both diffusive perturbations appear closer to the center of the phan-

tom than their true position. In this case, the linear reconstruction provides slightly better spatial resolution and positional accuracy than the nonlinear reconstruction.

### 3. Clear Perturbations and Ring

Figure 5 shows images reconstructed with both clear perturbations and a clear layer. When the homogeneous phantom is used as the reference [Fig. 5(a)], the nonlinear reconstruction can resolve both diffusive perturbations, but the image quality is poor. Linear reconstruction evidently fails.

When the reference data includes the clear layer and two clear regions [Fig. 5(b)], the nonlinear and the linear reconstructions perform qualitatively similarly. Neither manages to resolve the two diffusive features, but both identify increases in absorption and scatter.

### B. Head-Shaped Phantom

Transverse and sagittal slices through images obtained from the head-shaped phantom are shown in Fig. 6 and broadly agree with those from the cylindrical phantom. Both linear and nonlinear reconstruction techniques successfully generate simple difference images when two diffusing perturbations are inserted into a homogeneous, diffusive-only phantom, although there is significant cross talk in the optical parameters between the two cases. Once again, linear reconstruction gives slightly better spatial resolution than nonlinear [Fig. 6(a)], but nonlinear reconstruction separates the effect of absorption and scatter better than linear.

As in the cylindrical case, difference images reconstructed from data obtained with the head-shaped phantom with a clear shell and two central clear regions with and without two diffusive perturbations [Fig. 6(b)] seem qualitatively similar to the simple diffusive-only case, provided the clear regions are common to both the image data and the reference data. Again, in this case, which corresponds to the clinical situation of imaging before and after a physiological change, linear and, nonlinear reconstructions perform similarly.

When images are reconstructed with the same data but with a homogeneous phantom as a reference [corresponding clinically to static imaging using a fluid-filled balloon as a reference; see Fig. 6(c)], the nonlinear reconstruction seems to identify the two clear regions as regions of low scatter and low absorption and a single localized diffusive increase. The nonlinear images seem to represent the true distribution of optical properties more faithfully than was the case in the cylindrical phantom [Fig. 5(a)]. Linear images [Fig. 6(c)] failed to produce reliably localized features, but some common features between the linear and the nonlinear images can be seen, suggesting that the linear reconstruction did not fail completely, as was the case when data from the corresponding cylindrical phantom [Fig. 5(a)] were reconstructed.

## 4. Conclusion

### A. Effect of Void Regions

From the images presented in Figs. 3–5, we can examine two general cases: first, imaging a phantom containing clear regions when those regions *are* present in a reference image, and second, imaging the same phantom when the “un-model-able” regions *are not* present in the reference. Clinically, the first case is equivalent to functional imaging of an induced change,<sup>11</sup> whereas the second case is equivalent to static imaging with a homogeneous phantom as a reference.<sup>10</sup>

The first case can be seen in Figs. 3(c), 4(c), and 5(b), roughly in order of increasing complexity. In all cases, the increase in absorption and scatter due to the diffusive perturbations can be clearly seen in both the linear and the nonlinear reconstructions. Discrete clear regions [Fig. 3(c)] seem to distort the image less than the presence of a clear layer [Fig. 4(c)], although this could depend on the particular geometry of the clear regions used in this study. The presence of a clear layer seems to make the diffusive perturbations appear to be closer to the center of the image than their true position and reduces the ability of the reconstruction to distinguish between the two features, a result that is likely due to light being “piped” around the clear layer, thus avoiding deeper regions.

The second, more demanding, case is illustrated in Figs. 3(b), 4(a), 4(b), and 5(a). Here, the linear reconstruction fails (see Subsection 4.B), but the nonlinear reconstruction does produce images that seem reasonable. In Fig. 3(b), for example, the nonlinear reconstruction identified all four perturbations (including two void regions) correctly. As the complexity of the clear areas increased, however, the nonlinear reconstructions increasingly failed to distinguish between the individual perturbations correctly. Again, the presence of a clear layer seems to reduce the image quality more than central clear regions.

These observations may help resolve an apparent contradiction in the literature between the claims of some researchers who argue that light transport<sup>23,25</sup> and image reconstruction<sup>24,39,41</sup> are severely distorted by the presence of clear regions and those<sup>30,31</sup> who have observed little effect on the image reconstruction due to the clear regions. The results presented here support both positions: static imaging is highly sensitive to the presence of a clear layer, but dynamic imaging, where the clear layer is also present in a reference image, is much more robust. However, even when the presence of a clear region allows qualitatively plausible dynamic images,<sup>30,31</sup> the quantitation of the amplitude of the change in optical properties is poor, and it is difficult to foresee *quantitatively* accurate images being obtained without correctly modeling the optical properties of the entire medium. One further complication when comparing different studies is that the effect of the clear

layer will, of course, depend on the optical properties and geometry of each individual study.<sup>39,42</sup>

The effect of the clear regions seemed less severe in images reconstructed from the head-shaped phantom (Fig. 6) than the cylindrical phantom (Figs. 3–5). The reason for this is likely that light can be “piped” in a straight line through the clear cylindrical shell to the ends of the phantom and therefore not contribute usefully to the image reconstruction. In the head-shaped phantom, however, light that is “piped” around the clear spherical shell is more likely to diffuse back to the detector and contribute to a measurement. This issue is being examined further.

#### B. Linear and Nonlinear Image Reconstruction

A dramatic difference in performance between linear and nonlinear reconstruction can be seen by comparing those figures for which the reference included the void regions [Figs. 3(c), 4(c), and 5(b)] with those for which the reference was homogeneous [Figs. 3(b), 4(a), 4(b) and 5(a)]. For the first group, linear reconstruction seemed to perform qualitatively as well as nonlinear reconstruction, while for the second group, linear reconstruction failed. This result supports part of the hypothesis proposed in Section 1, which postulated that linear reconstruction was most appropriate when there was a small change in optical properties from an unknown or “un-model-able” background. Nonlinear reconstruction, on the other hand, seemed to perform similarly well whether the background was known and “model-able” or not.

Our results suggest that in practice, even though nonlinear reconstruction may provide similar or even better quality images, linear reconstruction might be justified when a small change is being imaged and that reconstruction speed is an issue, as is often the case in optical topography.

#### C. Other Approaches

Of course, the degradation in image quality due to the clear regions would disappear if light transport in those regions could be modeled sufficiently accurately, for instance, by use of the radiative transport equation rather than the diffusion approximation.<sup>1</sup> Several groups are working on this problem, but computational speed is still a limiting factor, and image reconstruction of a head-sized 3D volume, including realistic void regions has not yet been demonstrated.

Monte Carlo techniques can precisely simulate the effect of clear regions,<sup>42–44</sup> but the computational time required is prohibitively long for these methods to be used in image reconstruction in the foreseeable future. The method of discrete ordinates makes the computational demands of the radiative transport equation tractable by discretizing in both direction and space. This method<sup>45</sup> has been used successfully<sup>46</sup> for small objects such as the finger, and for coarse directional discretization. A coupled radiosity-diffusion model has been developed at UCL that models light transport in scattering regions with the diffusion model, and in clear regions with a visibility

model of geometrical optics. Currently, the model can be applied to 2D and some 3D geometries,<sup>47</sup> but it has not yet been applied to a headlike model.

It is likely that in the near future, it will be possible to obtain accurate models of the clear regions of the head, provided the geometry of those regions is known. Meanwhile, diffusion-only models or simple radiative transport models will continue to be used for *in vivo* imaging, particularly in topographic systems. This work supports the use of such an approach, provided that the nonscattering regions are common to the image and the reference data sets.

#### D. Implications for Imaging the Human Brain

The results of this investigation, particularly the images shown in Fig. 6, suggest that the effect of nonscattering regions on human brain imaging largely depends on whether the clear regions are included in a reference measurement. Where the clear regions are included, such as in optical topography and tomography of physiological changes in the brain, changes in absorption and scatter can be identified, although this work does not provide enough data to determine the likely quantitative accuracy of the images. If the clear regions are not present in the reference image, useful images can still be obtained, but they need to be interpreted with care. In particular, it must be suspected that any decreases in absorption and scatter that are observed in an image originate in the clear regions in the head and not from other features of interest. However, this work does provide some support for the use of a homogenous diffusive-only phantom for imaging a large increase in absorption such as a hemorrhage.<sup>10</sup>

In the real clinical case, the clear regions have boundaries that are not smooth. This may reduce the effect of light “piping” in straight lines, and consequently the distortion in the image.<sup>41,48</sup> Furthermore, in the pathological brain, the CSF is not necessarily clear—more than 90% of patients who have a subarachnoid hemorrhage have blood or blood products in their CSF, which then appears turbid, and normal CSF in newborn babies often contains blood products.<sup>49</sup>

The authors thank Hamid Dehghani for providing a program to calculate the sensitivity matrix used in this work and the Wellcome Trust and EPSRC for their support.

#### References

1. S. R. Arridge, “Optical tomography in medical imaging,” *Inverse Probl.* **15**, R41–R93 (1999).
2. J. C. Hebden, S. R. Arridge, and D. T. Delpy, “Optical imaging in medicine: I. Experimental techniques,” *Phys. Med. Biol.* **42**, 825–840 (1997).
3. D. A. Boas, D. H. Brooks, E. L. Miller, C. A. DiMarzio, M. Kilmer, R. J. Gaudette, and Q. Zhang, “Imaging the body with diffuse optical tomography,” *IEEE Signal Processing Mag.* **18**, 57–75 (2001).
4. D. Grosenick, K. T. Moesta, H. Wabnitz, J. Mucke, C. Stroszynski, R. Macdonald, P. M. Schlag and H. Rinneberg, “Time-domain optical mammography: initial clinical results on

- detection and characterization of breast tumors," *Appl. Opt.* **42**, 3170–3186 (2003).
5. M. J. Holboke, B. J. Tromberg, X. Li, N. Shah, J. B. Fishkin, D. Kidney, J. Butler, B. Chance, and A. G. Yodh, "Three-dimensional diffuse optical mammography with ultrasound localization in a human subject," *J. Biomed. Opt.* **5**, 237–247 (2000).
  6. H. Dehghani, B. W. Pogue, S. P. Poplack, and K. D. Paulsen, "Multiwavelength three-dimensional near-infrared tomography of the breast: initial simulation, phantom and clinical results," *Appl. Opt.* **42**, 135–145 (2003).
  7. J. C. Hebden, T. Bland, E. M. C. Hillman, A. P. Gibson, N. Everdell, D. T. Delpy, S. R. Arridge, and M. Douek, "Optical tomography of the breast using a 32-channel time-resolved imager," in *Digest of OSA Biomedical Topical Meetings* (Optical Society of America, Washington, D.C., 2002), 187–189.
  8. A. Li, E. L. Miller, M. Kilmer, T. J. Brukilacchio, T. Chaves, J. J. Stott, Q. Zhang, T. Wu, M. Chorlton, R. H. Moore, D. B. Kopans, and D. A. Boas, "Tomographic optical breast imaging guided by three-dimensional mammography," *Appl. Opt.* **42**, 5181–5190 (2003).
  9. D. A. Benaron, S. R. Hintz, A. Villringer, D. A. Boas, A. Kleinschmidt, J. Frahm, C. Hirth, H. Obrig, J. C. van Houten, E. L. Kermit, W.-F. Cheong, and D. K. Stevenson, "Noninvasive functional imaging of human brain using light," *J. Cereb. Blood Flow Metab.* **20**, 469–477 (2000).
  10. J. C. Hebden, A. P. Gibson, R. M. Yusof, N. Everdell, E. M. Hillman, D. T. Delpy, T. Austin, J. Meek, and J. S. Wyatt, "Three-dimensional optical tomography of the premature infant brain," *Phys. Med. Biol.* **47**, 4155–4166 (2002).
  11. J. C. Hebden, A. P. Gibson, T. Austin, R. M. Yusof, N. Everdell, D. T. Delpy, S. R. Arridge, J. H. Meek, and J. S. Wyatt, "Imaging changes in blood volume and oxygenation in the newborn infant brain using three-dimensional optical tomography," *Phys. Med. Biol.* **49**, 1117–1130 (2004).
  12. A. Y. Bluestone, G. Abdoulev, C. H. Schmitz, R. L. Barbour, and A. H. Hielscher, "Three-dimensional optical tomography of hemodynamics in the human head," *Opt. Express* **9**, 272–286 (2001).
  13. M. A. Franceschini, V. Toronov, M. E. Filiaci, E. Gratton, and S. Fantini, "On-line optical imaging of the human brain with 160 ms temporal resolution," *Opt. Express* **6**, 49–57 (2000).
  14. B. Chance, E. Anday, S. Nioka, S. Zhou, L. Hong, K. Worden, C. Li, T. Murray, Y. Ovetsky, D. Pidikiti, and R. Thomas, "A novel method for fast imaging of brain function, non-invasively, with light," *Opt. Express* **2**, 411–423 (1998).
  15. J. C. Hebden, "Advances in optical imaging of the newborn infant brain," *Psychophysiology* **40**, 501–510 (2003).
  16. L. Marti-Lopez, J. Bouza-Dominguez, J. C. Hebden, S. R. Arridge and R. A. Martinez-Celirio, "Validity Conditions for the radiative transfer equation," *J. Opt. Soc. Am. A* **20**, 2046–2056 (2003).
  17. F. F. Jöbsis, "Noninvasive infrared monitoring of cerebral and myocardial oxygen sufficiency and circulatory parameters," *Science* **198**, 1264–1267 (1977).
  18. A. D. Edwards, C. Richardson, M. Cope, J. S. Wyatt, D. T. Delpy, and E. O. R. Reynolds, "Cotside measurement of cerebral blood flow in ill newborn infants by near infrared spectroscopy," *Lancet* **332**, 770–771 (1988).
  19. J. Meek, M. Firbank, C. E. Elwell, J. Atkinson, O. Braddick and J. S. Wyatt, "Regional haemodynamic responses to visual stimulation in awake infants," *Pediatr. Res.* **42**, 840–843 (1998).
  20. G. Taga, Y. Konishi, A. Maki, T. Tachibana, M. Fujiwara, and H. Koizumi, "Spontaneous oscillation of oxy- and deoxy-hemoglobin changes with a phase difference throughout the occipital cortex of newborn infants observed using non-invasive optical topography," *Neurosci. Lett.* **282**, 101–104 (2000).
  21. S. R. Hintz, W. F. Cheong, J. P. van Houten, D. K. Stevenson, and D. A. Benaron, "Bedside imaging of intracranial hemorrhage in the neonate using light: comparison with ultrasound, computed tomography, and magnetic resonance imaging," *Pediatr. Res.* **45**, 54–59 (1999).
  22. G. Strangman, J. P. Culver, J. H. Thompson, and D. A. Boas, "A quantitative comparison of simultaneous BOLD fMRI and NIRS recordings during functional brain activation," *Neuroimage* **17**, 719–731 (2002).
  23. A. H. Hielscher, R. E. Alcouffe, and R. L. Barbour, "Comparison of finite difference transport and diffusion calculations for photon migration in homogeneous and heterogeneous tissues," *Phys. Med. Biol.* **43**, 1285–1302 (1998).
  24. H. Dehghani, D. T. Delpy and S. R. Arridge, "Photon migration in non-scattering tissue and the effects on image reconstruction," *Phys. Med. Biol.* **44**, 2897–2906 (1999).
  25. E. Okada, M. Firbank, M. Schweiger, S. R. Arridge, M. Cope and D. T. Delpy, "Theoretical and experimental investigation of near-infrared light propagation in a model of the adult head," *Appl. Opt.* **36**, 21–31 (1997).
  26. M. Firbank, S. R. Arridge, M. Schweiger, and D. T. Delpy, "An investigation of light transport through scattering bodies with non-scattering regions," *Phys. Med. Biol.* **41**, 767–783 (1996).
  27. J. D. Riley, S. R. Arridge, Y. Chrysanthou, H. Dehghani, E. M. Hillman, and M. Schweiger, "Radiosity diffusion model in 3D," in *Photon Migration, Optical Coherence Tomography, and Microscopy*, S. Andersson-Engels and M. F. Kaschke, eds., *Proc. SPIE* **4431**, 153–164 (2001).
  28. A. H. Hielscher and R. E. Alcouffe, "Non-diffusive photon migration in homogeneous and heterogeneous tissues," in *Photon Propagation in Tissue II*, B. Chance, D. Benaron, G. J. Müller, eds., *Proc. SPIE* **2925**, 22–30 (1996).
  29. H. Dehghani, S. R. Arridge, M. Schweiger, and D. T. Delpy, "Image reconstruction in the presence of a void region," in *Digest of OSA Biomedical Topical Meetings* (Optical Society of America, Washington, D.C. 2000), pp. 351–353.
  30. Y. Pei, H. L. Graber, and R. L. Barbour, "Normalized-constraint algorithm for minimizing inter-parameter crosstalk in DC optical tomography," *Opt. Express* **11**, 97–109 (2001).
  31. C. H. Schmitz, M. Locker, J. M. Lasker, A. H. Hielscher, and R. L. Barbour, "Instrumentation for fast functional optical tomography," *Rev. Sci. Instrum.* **73**, 429–439 (2002).
  32. S. R. Arridge, J. C. Hebden, M. Schweiger, F. E. W. Schmidt, M. E. Fry, E. M. C. Hillman, H. Dehghani, and D. T. Delpy, "A method for 3D time-resolved optical tomography," *Int. J. Imaging Syst. Technol.* **11**, 2–11 (2000).
  33. M. Firbank, M. Oda, and D. T. Delpy, "An improved design for a stable and reproducible phantom material for use in near-infrared spectroscopy and imaging," *Phys. Med. Biol.* **40**, 955–961 (1995).
  34. A. P. Gibson, R. M. Yusof, H. Dehghani, J. Riley, N. Everdell, R. Richards, J. C. Hebden, M. Schweiger, S. R. Arridge, and D. T. Delpy, "Optical tomography of a realistic neonatal head phantom," *Appl. Opt.* **42**, 3109–3116 (2003).
  35. F. E. W. Schmidt, J. C. Hebden, E. M. C. Hillman, M. E. Fry, M. Schweiger, H. Dehghani, D. T. Delpy, and S. R. Arridge, "Multiple-slice imaging of a tissue-equivalent phantom by use of time-resolved optical tomography," *Appl. Opt.* **39**, 3380–3387 (2000).
  36. J. C. Hebden, F. M. Gonzalez, A. P. Gibson, E. M. Hillman, R. M. Yusof, N. Everdell, D. T. Delpy, G. Zaccanti, and F. Martelli, "Assessment of an *in situ* temporal calibration method for time-resolved optical tomography," *J. Biomed. Opt.* **8**, 87–92 (2003).
  37. J. Schöberl, "NETGEN - An advancing front 2D/3D-mesh gen-

- erator based on abstract rules," *Comput. Visual. Sci.* **1**, 41–52 (1997).
38. A. P. Gibson, J. Riley, M. Schweiger, J. C. Hebden, S. R. Arridge, and D. T. Delpy, "A method for generating patient-specific finite element meshes for head modelling," *Phys. Med. Biol.* **48**, 481–495 (2003).
  39. H. Dehghani and D. T. Delpy, "Linear single-step image reconstruction in the presence of nonscattering regions," *J. Opt. Soc. Am. A* **19**, 1162–1171 (2002).
  40. M. Schweiger, S. R. Arridge, M. Hiraoka, and D. T. Delpy, "The finite element method for the propagation of light in scattering media: boundary and source conditions," *Med. Phys.* **22**, 1779–1792 (1995).
  41. H. Dehghani, S. R. Arridge, M. Schweiger, and D. T. Delpy, "Optical tomography in the presence of void regions," *J. Opt. Soc. Am. A* **17**, 1659–1670 (2000).
  42. E. Okada and D. T. Delpy, "Near-infrared light propagation in an adult head model. I. Modeling of low-level scattering in the cerebrospinal fluid layer," *Appl. Opt.* **42**, 2906–2914 (2003).
  43. D. A. Boas, J. P. Culver, J. J. Stott, and A. K. Dunn, "Three dimensional Monte Carlo code for photon migration through complex heterogeneous media including the adult human head," *Opt. Express* **10**, 159–169 (2002).
  44. T. Hayashi, Y. Kashio, and E. Okada, "Hybrid Monte Carlo-diffusion method for light propagation in tissue with a low-scattering region," *Appl. Opt.* **42**, 2888–2896 (2003).
  45. O. Dorn, "A transport-backtransport method for optical tomography," *Inverse Probl.* **14**, 1107–1130 (1998).
  46. A. D. Klose and A. H. Hielscher, "Iterative reconstruction scheme for optical tomography based on the equation of radiative transfer," *Med. Phys.* **28**, 1698–1707 (1999).
  47. J. Riley, H. Dehghani, M. Schweiger, S. R. Arridge, J. Ripoll, and M. Nieto-Vesperinas, "3D optical tomography in the presence of void regions," *Opt. Express* **7**, 462–467 (2000).
  48. J. Ripoll, M. Nieto-Vesperinas, and S. R. Arridge, "Effect of roughness in nondiffusive regions within biological media," *J. Opt. Soc. Am. A* **18**, 940–947 (2001).
  49. D. A. Seehusen, M. M. Reeves, and D. A. Fomin, "Cerebrospinal fluid analysis," *Am. Fam. Physician* **68**, 1103–1108 (2003).